ACS Sustainable Chemistry & Engineering

Research Article

Cite This: ACS Sustainable Chem. Eng. 2018, 6, 16055−16063

pubs.acs.org/journal/ascecg

Transformed Akhtenskite MnO_2 from Mn_3O_4 as Cathode for a Rechargeable Aqueous Zinc Ion Battery

Lulu Wang, Xi Cao, Linghong Xu, Jitao Chen,* and Junrong Zheng*

College of Chemistry and Molecular Engineering, Beijing National Laboratory for Molecular Sciences, Peking University, 202, Chengfu Road, Beijing 100871, P. R. China

Supporting Information

ABSTRACT: Low cost, safety, and environmental benignity make rechargeable aqueous Zn/MnO_2 batteries promising candidates for large-scale energy storage. However, the synthesis of MnO_2 with excellent electrochemical performance is limited to the traditional hydrothermal method, which is difficult to scale up for mass production. Herein, a ball-milling approach is developed to rapidly obtain Mn_3O_4 nanoparticles in large quantity. As the cathode material of aqueous zinc ion battery, Mn_3O_4 gradually transforms to ε-MnO_2 in 1 M $ZnSO_4$ + 1 M $MnSO_4$ aqueous electrolyte with increasing cycles. Benefiting from the unexpected phase transition from Mn_3O_4 to ε-MnO_2, the cathode delivers a specific capacity of 221 mAh g^{-1} at a current density of 100 mA g^{-1} and a good long-term cyclic stability over 500 cycles with 92% capacity retention at a high rate of 500 mA g^{-1}. The excellent battery performance combined with the cost-effective preparation procedure, the good safety of aqueous mild electrolyte, and the easy cell assembly are believed to promote the practical use of the Zn/MnO_2 battery in large-scale energy storage.

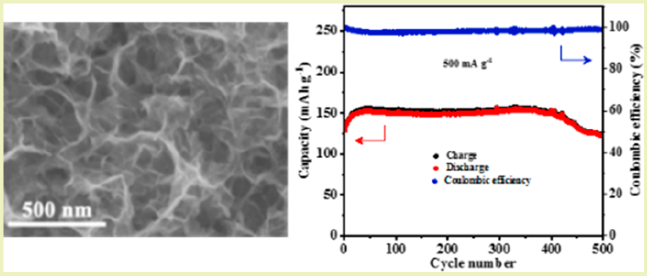

KEYWORDS: *Aqueous zinc ion battery, Ball-milled Mn_3O_4, Electrochemical phase transition, MnO_2 nanosheet, H^+ intercalation and deintercalation*

INTRODUCTION

There is an ever increasing demand for large-scale electrochemical energy storage systems with low cost and environmental benignity due to the rapid increase in climate change and environmental pollution. Many types of rechargeable batteries have been under development, e.g., lithium ion batteries (LIBs) and traditional lead−acid batteries. LIBs with relatively high energy density compared to other secondary batteries can meet the demands of a wide range of applications, including portable electronics, electric vehicles, and large-scale grid applications.[1−3] However, their large-scale applications are plagued by high cost, poor safety, potential resource shortage, and environmental concerns.[4−8] On the other hand, lead−acid batteries are relatively low-cost aqueous systems and much easier to scale up for various applications. Nevertheless, in addition to the low energy density and limited life span, the utilization of lead brings about severe environmental issues. Extensive efforts have been dedicated to looking for promising candidates to address these challenges. Rechargeable aqueous batteries employing water-based electrolytes with higher ionic conductivity,[9−11] better safety, and simpler fabrication process are gaining increasing attention. In particular, rechargeable aqueous Zn ion batteries (ZIBs) based on Zn ion intercalation/extraction are considered as attractive alternatives due to the high abundance of Zn,[12,13] environmental friendliness,[14] multivalent charge transport carriers, relatively low redox potential (−0.76 V vs standard hydrogen electrode),[10] and high theoretic gravimetric capacity (825 mAh g^{-1}).[15] To date, two main types of cathode materials have been explored for reversible Zn ion intercalation/deintercalation, the Prussian Blue family, such as zinc hexacyanoferrate[16,17] and copper hexacyanoferrate,[18−22] and polymorphic (α, β, γ, δ, λ, and amorphous) MnO_2.[23−30] The former materials exhibit limited capacities, and the latter suffer severe capacity fading in mild aqueous electrolytes. Recently, the cyclic stability of an aqueous Zn/MnO_2 battery was significantly improved by adding Mn^{2+} to the electrolyte, rendering an electrochemical equilibrium between Mn^{2+} dissolution from the electrode to the electrolyte and the reoxidation of Mn^{2+} in the electrolyte.[31,32] With no doubt, the extended life span sheds light on the realization and development of practical rechargeable aqueous ZIBs. However, the cathode materials, different forms of MnO_2 with excellent electrochemical performance, are almost exclusively synthesized via the traditional hydrothermal method,[31,32] which would be extremely costly to continuously produce or scale up. Hence, rechargeable aqueous ZIBs are far from meeting the demands essential for large-scale applications. In this regard, it is still very challenging to explore new reversible cathode

Received: May 31, 2018
Revised: September 22, 2018
Published: October 30, 2018

ACS Publications

DOI: 10.1021/acssuschemeng.8b02502

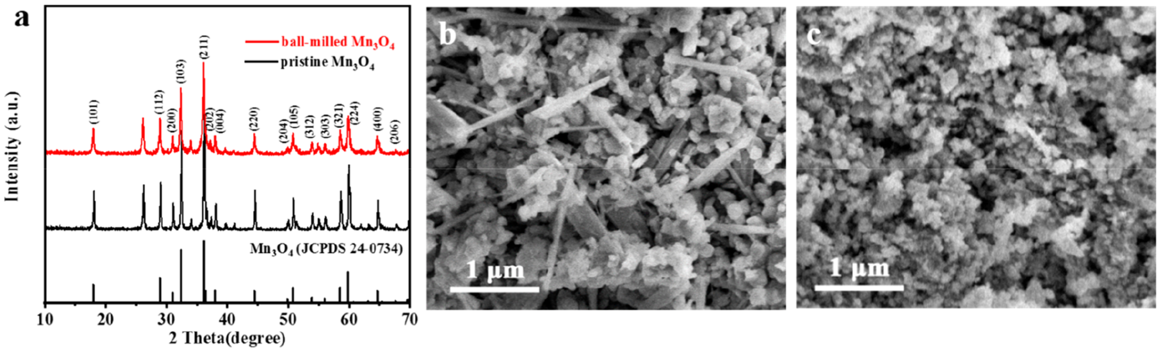

Figure 1. Materials characterization of Mn_3O_4. (a) XRD patterns and (b and c) SEM images of pristine Mn_3O_4 and ball-milled Mn_3O_4, respectively.

materials with high capacity and long-term cycling stability that are readily available in large quantities.

In this study, we develop a ball-milling approach to rapidly prepare Mn_3O_4 nanoparticles of around 150 nm in large quantity. The Mn_3O_4 raw material can be obtained in bulk at the price of 13 000 RMB (about 2000 USD) per ton, and a nano-Mn_3O_4 cathode can be obtained by a facile ball-milling method in large scale. We can prepare 150 g of uniformly ball-milled Mn_3O_4 nanoparticles in 2 h, as shown in Figure S1 (Supporting Information, SI). To prepare an equal-quality cathode, the cost of the hydrothermal method in previous reports[31,32] is about 25 times more than ball-milling method. Moreover, the hydrothermal method takes more than 12 h, nearly 6 times as long as the ball-milling method. In addition, without cooling, centrifugation, and washing, the ball-milling method is much simpler than the hydrothermal method. Last but not least, the traditional hydrothermal method is plagued with discontinuous production and poor repeatability stemming from strict control of the reaction temperature and time. Thus, compared to the traditional hydrothermal method, the ball-milling method has overwhelming superiority in preparation cost and time.

An aqueous battery is assembled with the milled Mn_3O_4 nanoparticles as cathode and Zn as anode in a 1 M $ZnSO_4$ + 1 M $MnSO_4$ aqueous electrolyte. Because of an unexpected phase transition from spinel Mn_3O_4 to ε-MnO_2 during cycling, the cathode delivers a high specific capacity of 221 mAh g^{-1} at a current density of 100 mA g^{-1} and exhibits excellent long-term cyclic stability with 92% capacity retention after 500 cycles at 500 mA g^{-1}. Furthermore, the electrochemical reaction mechanism of ε-MnO_2 electrode is investigated by means of electrochemical measurements combined with ex situ X-ray diffraction (XRD), ex situ X-ray photoelectron spectroscopy (XPS), scanning TEM/energy dispersive spectroscopy (STEM−EDS) mapping, and transmission electron microscopy (TEM).

EXPERIMENTAL SECTION

Material Preparation. Spinel Mn_3O_4 of 150 nm was prepared through the ball-milling process. The Mn_3O_4 (Macklin, 97%) was added into ethanol to form a paste. This paste was ball-milled using zirconia milling media in a planetary ball mill at a rotation speed of 2000 rpm for 2 h. After ball milling, the mixture was dried at 80 °C to evaporate ethanol. The Mn_3O_4 powder obtained after thorough grinding was used for further characterization. The facile preparation is feasible for mass production (Figure S1, SI).

Characterizations. The crystalline structure of the electrode was characterized by XRD (Rigaku Dmax/2400 diffractometer with Cu Kα radiation, 40 kV, 100 mA). The morphology analysis before and after electrochemical cycling was carried out using field emission scanning electron microscopy (FE-SEM) (S4800, Hitachi) and TEM (JEM-2100F, JEOL) equipped with energy dispersive spectroscopy (EDS) for elemental analysis. The oxidation states of Mn in cathodes were analyzed by XPS (Axis Ultra, Kratos Analytical Ltd.). All binding energy values were referenced to the C 1s peak of carbon at 284.8 eV.

Electrochemical Measurements. Electrochemical measurements of the cathode were performed using CR2032 coin-type cells. The composite cathode was first fabricated by making a slurry containing 70 wt % spinel Mn_3O_4, 20 wt % conductive graphite (TIMCAL KS6), and 10 wt % poly(vinylidene difluoride) (PVDF) in 1-methyl-2-pyrrolidinone (NMP). The slurry was then cast onto stainless steel (SUS 304) mesh, followed by drying at 70 °C in a vacuum oven. The mass load of the active material in each electrode was 2 mg cm^{-2}. Full coin cells were assembled with the Mn_3O_4 as cathode, Zn sheet as anode, and glass fiber sheet as separator, respectively. A 1 M $ZnSO_4$ + 1 M $MnSO_4$ aqueous solution was employed as the electrolyte solution. For comparison, the performance of the cathode was also tested in 1 M $ZnSO_4$, 1 M $ZnSO_4$ + 0.2 M $MnSO_4$, 1 M $ZnSO_4$ + 0.4 M $MnSO_4$, and 1 M $ZnSO_4$ + 0.7 M $MnSO_4$ aqueous electrolytes.

Galvanostatic discharge−charge tests were conducted on a LAND-CT2001A battery test system. Calculation of current density and specific capacity was based on the mass of Mn_3O_4 in each electrode. The coin cells were galvanostatically cycled at 100 mA g^{-1} in the potential range of 0.6 and 1.9 V for 10 cycles. As electrochemical cycling proceeded in the aqueous electrolyte, spinel Mn_3O_4 was gradually transformed to MnO_2. The cyclic voltammetry (CV) testing of the transformed MnO_2 cathode was conducted on a CHI660E electrochemical workstation between 0.6 and 1.9 V at a scan rate of 0.1 mV s^{-1}. Electrochemical impedance spectroscopy (EIS) was carried out on a CHI660E electrochemical workstation with an ac voltage of 5 mV amplitude over a frequency range from 0.1 Hz to 1 MHz. Symmetrical Zn/Zn cells with two Zn foils as working and counter electrodes were assembled to test the electrochemical reversibility and stability of 45 wt % KOH, 1 M $ZnSO_4$, and 1 M $ZnSO_4$ + 1 M $MnSO_4$ aqueous electrolytes, respectively. All the electrochemical measurements were carried out at room temperature.

RESULTS AND DISCUSSION

Electrochemical Phase Transformation of Cathode.

The structure, crystalline size, and morphology of the cathode material Mn_3O_4 are characterized by means of XRD and SEM Figure 1a displays XRD patterns of pristine (as received) and ball-milled Mn_3O_4. X-ray peaks of ball-milled product are readily indexed to Mn_3O_4 (JCPDS 24-0734), indicating that the crystal structure of pristine Mn_3O_4 is well-preserved. Peaks of the milled sample are broader in comparison to those of pristine Mn_3O_4, resulting from the smaller size and larger

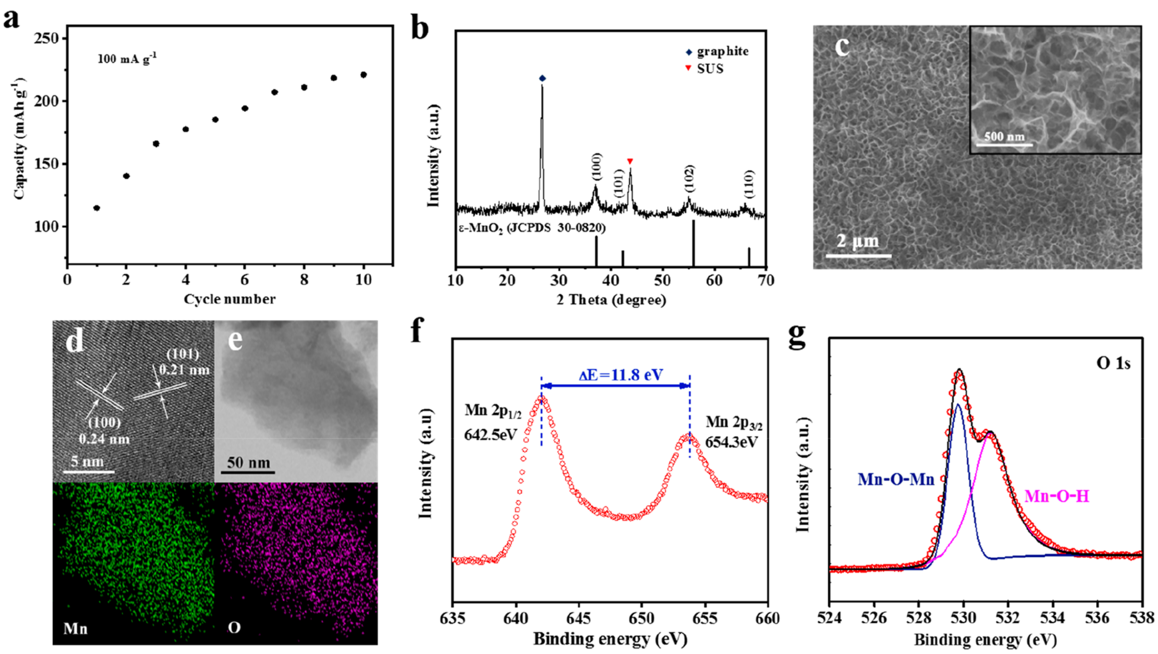

Figure 2. Aqueous phase transition from spinel Mn_3O_4 to ε-MnO_2 and material characterizations of the transformed ε-MnO_2 cathode. (a) Discharge capacities of ball-milled Mn_3O_4 with 150 nm dimension at 100 mA g^{-1} in 1 M $ZnSO_4$ + 1 M $MnSO_4$ aqueous electrolyte. (b) The XRD pattern. (c) SEM images. (d) HRTEM images. (e) STEM micrograph with elemental mapping images. (f) Mn 2p XPS spectrum and (g) O 1s XPS spectrum of the cathode after 10 cycles. (In XPS spectra: red circle, experimental data; black line, overall fitted data; other colored lines, fitted individual components.)

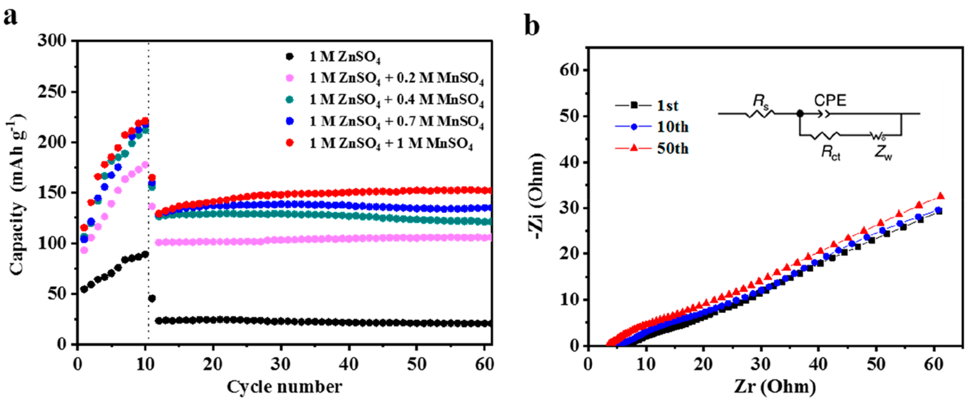

Figure 3. (a) Electrochemical performances of Zn/Mn_3O_4 cells using different electrolytes. (b) EIS spectra of the Zn/ε-MnO_2 cell after the 1st, 10th, and 50th charge at 500 mA g^{-1} in 1 M $ZnSO_4$ + 1 M $MnSO_4$ aqueous electrolyte in the frequency range of 0.1−100 000 Hz and the corresponding fitting equivalent circuit (inset).

surface area. The SEM image (Figure 1c) of ball-milled Mn_3O_4 reveal that spinel particles are uniform and are around 150 nm.

A coin cell was assembled and tested with the milled Mn_3O_4 as cathode, Zn sheet as anode, and 1 M $ZnSO_4$ + 1 M $MnSO_4$ aqueous solution as electrolyte. Intriguingly, galvanostatically cycled at the current density of 100 mA g^{-1}, the specific capacity of the cell (calculated on the basis of the cathode mass) increases continuously for more than 100% and reaches 221 mAh g^{-1} after 10 cycles, as displayed in Figure 2a. The surprising capacity change was further investigated by comprehensively characterizing the cathode after activation for 10 cycles. Figure 2b displays the XRD pattern of the activated cathode. The X-ray diffraction peaks are well-indexed to akhtenskite MnO_2 (JCPDS 30-0820) and peaks belonging to the spinel Mn_3O_4 disappear, demonstrating that the spinel Mn_3O_4 has transformed into ε-MnO_2 after activation. Accompanying the phase transition, the morphology of the cathode material changes from the irregular nanoparticle shape (Figure 1b) to a porous structure consisting of interconnected nanosheets with a thickness of ∼10 nm (Figure 2c). The porous MnO_2 nanosheets with large specific area provide abundant interfaces for electrode/electrolyte contact, resulting in fast electrochemical redox kinetics to achieve better reversibility during the charge and discharge processes. The measured lattice fringes of 0.24 and 0.21 nm in high-resolution transmission electron microscopy (HRTEM) images (Figure 2d) correspond to the (100) and (101) crystal planes of ε-MnO_2, which match the XRD results very well. Moreover, the nanosheet structure is relatively homogeneous, and Mn and O are uniformly distributed in the nanosheets, as suggested by the representative TEM image and STEM-EDS mapping images (Figure 2e).

In addition, XPS analysis was performed to confirm the oxidation state of Mn and the electronic structure of the

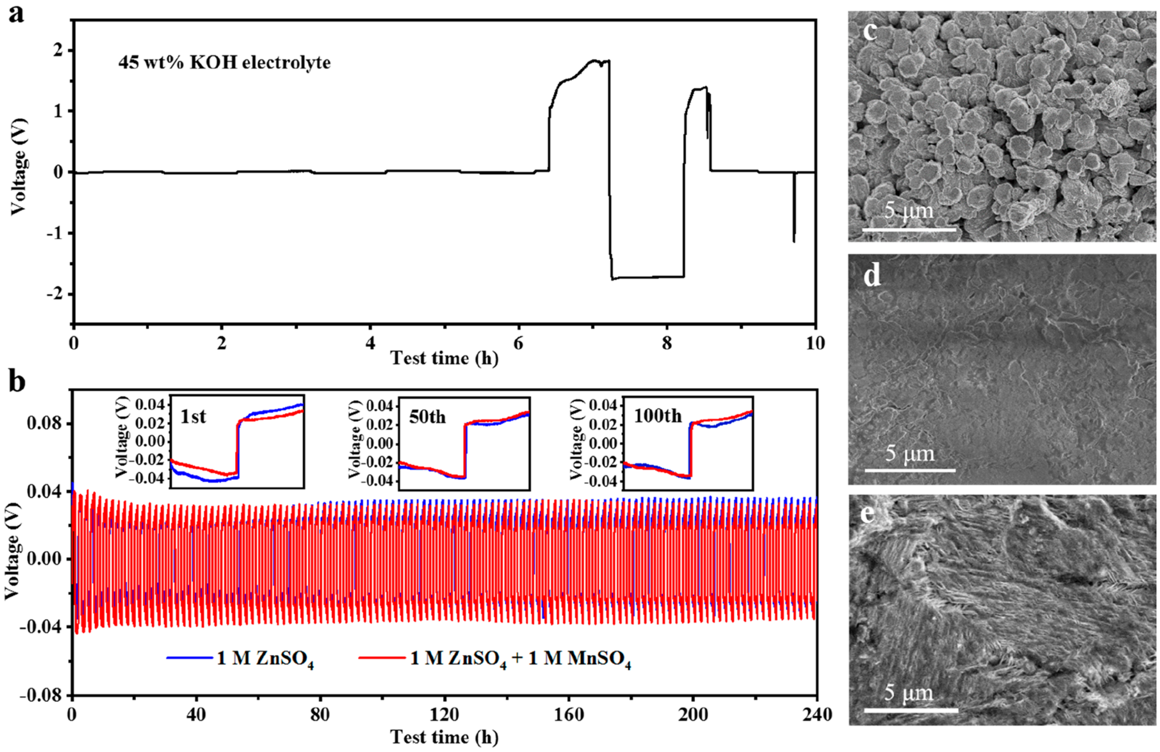

Figure 4. Zn stripping/plating from the Zn/Zn symmetrical cells at 0.1 mA cm^{-2} in (a) 45 wt % KOH aqueous electrolyte and (b) 1 M $ZnSO_4$ and 1 M $ZnSO_4$ + 1 M $MnSO_4$ aqueous electrolytes. Insets: characteristic charge and discharge voltage profiles of the 1st, 50th, and 100th cycle. SEM images of Zn anodes after Zn plating/stripping tests in (c) 45 wt % KOH, (d) 1 M $ZnSO_4$, and (e) 1 M $ZnSO_4$ + 1 M $MnSO_4$ aqueous electrolytes.

activitated cathode. The high-resolution Mn 2p spectrum (Figure 2f) shows two major peaks centered at 642.5 eV for Mn $2p_{3/2}$ and 654.3 eV for Mn $2p_{1/2}$, with a spin-energy separation of 11.8 eV, which are in good agreement with the previous reports for MnO_2,[33−35] indicating that the predominant oxidation state is +4 for the MnO_2 nanosheets. As shown in Figure 2g, the O 1s spectrum of activated cathode can be fitted with two components. According to the literature,[36] the fractional peaks at 529.5 and 531.5 eV can be attributed to the Mn−O−Mn bond for the tetravalent oxide and the Mn−O−H bond for hydrated trivalent oxide, respectively. The comprehensive results reveal that Mn_3O_4 transforms to MnO_2 after 10 aqueous electrochemical cycles.

Electrolyte Formulation. The electrochemical performance of Zn/Mn_3O_4 cell in different electrolytes are compared in Figure 3a. The cells employing different electrolytes were cycled at a low current density of 100 mA g^{-1} for 10 cycles to reach a stable state and then cycled at 500 mA g^{-1}. The specific capacity of the Zn/Mn_3O_4 cell utilizing 1 M $ZnSO_4$ electrolyte reaches 89 mAh g^{-1} at 100 mA g^{-1} after 10 cycles and delivers a capacity of no more than 30 mAh g^{-1} at 500 mA g^{-1}. The SEM image (Figure S2a, SI) shows that there are a few nanosheets on the surface of the Mn_3O_4 particles, which are responsible for the capacity. The predominant XRD peaks of the 10th fully charged cathode still belong to Mn_3O_4 (Figure S3, SI). However, with the $MnSO_4$ additive into the electrolyte, the discharge capacity of the cathode is significantly improved and the initial activation is clearly visible. In the case of 1 M $ZnSO_4$ + 0.2 M $MnSO_4$ electrolyte, the discharge capacity increases to 178 mAh g^{-1} at 100 mA g^{-1} after 10 cycles and delivers a capacity of 103 mAh g^{-1} at 500 mA g^{-1}. The SEM image of its activated cathode (Figure S4a, SI) presents a morphology of nanosheets similar to that in 1 M $ZnSO_4$ + 1 M $MnSO_4$ electrolyte (Figure 2c). The XRD data shows that both ε-MnO_2 and Mn_3O_4 are present in the activated cathode (Figure S5a, SI), demonstrating that the phase transition is not complete. With the increasing concentration of $MnSO_4$ additive, the discharge capacity increases to 221 mAh g^{-1} after activation. The cell employing 1 M $ZnSO_4$ + 1 M $MnSO_4$ electrolyte exhibits the highest specific capacity of 143 mAh g^{-1} at the current density of 500 mA g^{-1} and the best cycling stability. Therefore, the optimized electrolyte formulation is determined to be 1 M $ZnSO_4$ + 1 M $MnSO_4$, which is in favor of a thorough phase transition from Mn_3O_4 to ε-MnO_2 and cycling stability.

Figure 3b displays the electrochemical impedance spectroscopy (EIS) of Zn/ε-MnO_2 coin cell employing 1 M $ZnSO_4$ + 1 M $MnSO_4$ aqueous electrolyte at 500 mA g^{-1}. The Nyquist plot of the first cycle consists of one depressed semicircle in the high-frequency region and one line in the low-frequency area. From the corresponding fitting equivalent circuit (inset of Figure 3b), R_s, R_i, R_{ct}, CPE, and Z_w represent solution resistance, interface resistance between electrolyte and deposited layer, charge-transfer resistance, constant-phase element, and Warburg impedance, respectively. In addition, the EIS plots of the 10th and 50th cycle nearly coincide with that of the first cycle, indicating that the impedance of the Zn/ε-MnO_2 cell remains stable during cycling.

The series of experiments demonstrate the importance of Mn^{2+} for the phase transition from Mn_3O_4 to ε-MnO_2. Recently, the transformation of spinel Mn_3O_4 to crystal-water-containing layered birnessite MnO_2 during electrochemical cycling was reported in aqueous 1 M Li_2SO_4, 1 M Na_2SO_4, and 1 M $MgSO_4$ electrolyte solutions.[37−41] The mechanism was discussed elaborately. The anomalous spinel-to-layered phase transition is initiated by Mn^{2+} dissolution, accompanied by the

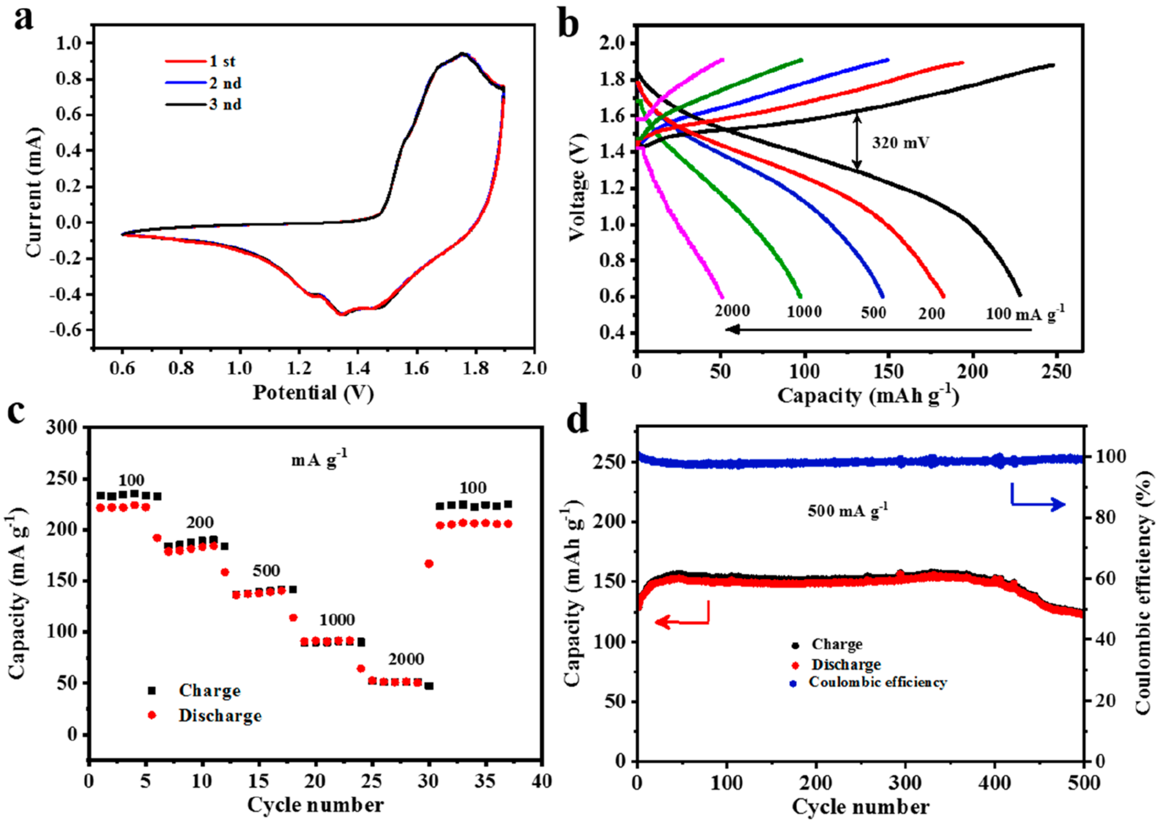

Figure 5. Electrochemical performance of the Zn /ε-MnO_2 coin cells. (a) Cyclic voltammetric (CV) curves of the Zn /ε-MnO_2 cell at a scan rate of 0.1 mV s^{-1}. (b) The discharge−charge voltage profiles at various current densities between 0.6 and 1.9 V. (c) Rate capability. (d) Long-term cyclic performance and the corresponding Coulombic efficiency at 500 mA g^{-1}.

oxidation and rearrangement of Mn^{3+} and the chemical insertion of H_3O^+ into the interlayer space during charge.[40,41]

The bare and hydrated radii (0.81−0.97 Å, 4.38 Å) and ionic hydration energy (−1860.1 kJ/mol) of Mn^{2+} are close to those (0.86 Å, 4.28 Å, −1923.4 kJ/mol) of Mg^{2+}.[42,43] The similarity may render similar ability for both cations to transport into and out of the crystal, therefore resulting in similar discharge capacities. However, different from Mg^{2+}, the final product of the phase transformation in Mn^{2+} solutions is ε-MnO_2 nanosheet rather than layered birnessite. The difference is probably because the presence of Mn^{2+} in the solution affects the dissolution equilibrium and kinetics of Mn^{2+} from the cathode during charging. The underlying mechanism of the phase transition is unclear and subject to future research.

To investigate the intrinsic properties of electrolytes, Zn plating/stripping tests of aqueous electrolytes were performed in Zn/Zn symmetric cells. Figure 4 illustrates the stability and reversibility of the Zn/Zn symmetric cell in alkaline electrolyte and mild aqueous electrolytes. In 45 wt % KOH electrolyte, severe polarization of Zn stripping/plating is observed after only 6 h. The XRD pattern (Figure S6, SI) and SEM image (Figure 4c) confirm the formation of ZnO nanorods, which hinders the reversibility of the Zn/Zn symmetric cell. The stability and reversibility of the Zn/Zn symmetric cell employing 1 M $ZnSO_4$ + 1 M $MnSO_4$ aqueous electrolyte are compared in Figure 4b. Charge/discharge curves are both smooth and cell voltages fluctuate within a narrow voltage range (±0.04 V) during cycling. The enlarged curves (Figure 4b, inset) overlap very well with the increasing cycles, demonstrating that the $MnSO_4$ additive in the $ZnSO_4$ aqueous electrolyte makes no difference in reversibility. Moreover, the cycled Zn anode in 1 M $ZnSO_4$ + 1 M $MnSO_4$ electrolyte exhibits a dense and smooth surface (Figure 4e). The XRD result of the Zn anode shows only the diffraction peaks of Zn, even after 120 cycles (Figure S6, SI).

Electrochemical Performance. To evaluate the electrochemical performance, coin cells were fabricated with ball-milled Mn_3O_4 cathode, Zn foil anode, glass fiber separator, and 1 M $ZnSO_4$ + 1 M $MnSO_4$ aqueous electrolyte.

The assembled coin cells were galvanostatically cycled at a low current density of 100 mA g^{-1} for 10 cycles to make Mn_3O_4 transform to ε-MnO_2. For 1 M $ZnSO_4$ + 1 M $MnSO_4$ electrolyte (pH ∼3.2), the O_2 evolution potential was suppressed up to 2.5 V and the H_2 evolution potential shifted below −0.05 V (vs Zn^{2+}/Zn) (Figure S7, SI). The working voltage window for our Zn/ε-MnO_2 cells is 0.6−1.9 V (vs Zn^{2+}/Zn). It is interesting to note that the potential range 1.3 V is higher than the decomposition voltage of water (1.23 V), but there are no detectable side reactions. The reason is relatively straightforward. The LUMO and HUMO potential of the electrolyte is −0.05 and 2.5 V, respectively. The electrochemical window of the electrolyte achieves 2.55 V (vs Zn^{2+}/Zn) (Figure S7, SI), which is higher than the decomposition voltage of water (1.23 V). Obviously, the potential range of 1.3 V (0.6−1.9 V vs Zn^{2+}/Zn) is located in the electrochemical window of the electrolyte (−0.05 to 2.5 V), so no detectable side reaction is expected. Figure 5 presents the electrochemical performances of the Zn/ε-MnO_2 cell after activation. Cyclic voltammetry (CV) curves between 0.6 and 1.9 V (vs Zn^{2+}/Zn) at a scan rate of 0.1 mV s^{-1} are

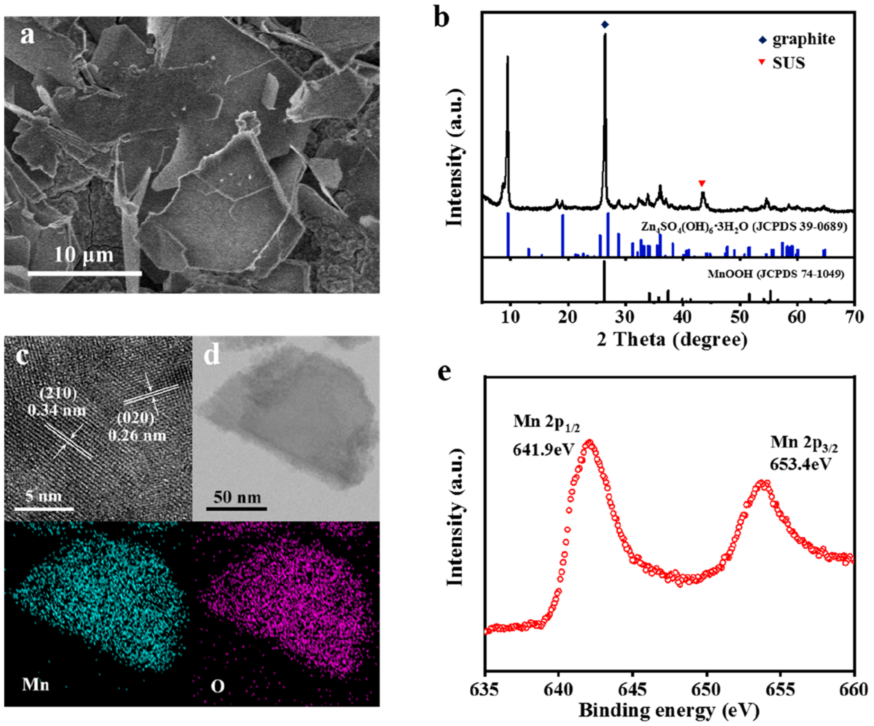

Figure 6. Characterizations of the fully discharged cathode. (a) SEM image. (b) XRD pattern. (c) HRTEM image. (d) Elemental mapping in STEM. (e) Mn 2p region of the XPS spectrum.

displayed in Figure 5a. A pair of redox peaks appears at 1.7 and 1.32 V, which are consistent with the plateaus in the charge/discharge curves shown in Figure 5b. The broad oxidation peak centered at around 1.7 V in cathodic sweeping can be attributed to H^+ extraction during the charge process. Accordingly, the reduction peak at 1.32 V in anodic scanning corresponds to intercalation of H^+ into the cathode during discharge. Besides, the CVs of the Zn/ε-MnO_2 cell remain invariable after the initial cycle, demonstrating the good reversibility of the ε-MnO_2 electrode. Figure 5b displays the discharge−charge voltage profiles of the Zn/ε-MnO_2 cell at various current densities in the voltage range of 0.6−1.9 V. The average discharge voltage plateaus of the discharge−charge voltage profile at 100 mA g^{-1} can be observed at 1.32 V, and the corresponding energy density is about 288 Wh kg^{-1} based on the active mass only. The polarization during charge/discharge is taken roughly as the voltage difference between the middle point of voltage profiles. The significant voltage difference of 320 mV can be seen even at a low current density of 100 mA g^{-1} (Figure 5b), which has also been observed and discussed for MnO_2 cathode in an aqueous Zn ion battery[31] and other conversion reactions from metal oxides electrode materials in lithium ion batteries.[44,45] The voltage difference at a low current could be attributed to a thermodynamic factor. First, the structure and morphology of cathode surface evolves from original porous interconnected MnO_2 nanosheets (Figure 3c) to MOOH nanosheets covered with disordered $ZnSO_4[Zn(OH)_2]_3{\cdot}3H_2O$ micrometer-sized flakes (Figure 6a) after discharge, which adds extra surface energy to the Gibbs free energy of the cathode. Second, other thermodynamic factors, such as the volume and surface energy variations during charge/discharge processes in the cathode, also account for the significant polarization at a low current density. The rate capability of transformed ε-MnO_2 cathode is shown in Figure 5c, where the current density is gradually increased from 100 to 2000 mA g^{-1} and abruptly returns to 100 mA g^{-1}. The cathode delivers average discharge capacities of 221, 182, 132, 91, and 51 mAh g^{-1} at current densities of 100, 200, 500, 1000, and 2000 mA g^{-1}, respectively. Remarkably, when the current density is reduced to 100 mA g^{-1}, the discharge capacity recovers to 203 mAh g^{-1}, revealing the considerable tolerance and good rate capability of the ε-MnO_2 cathode. At a low rate of 100 mA g^{-1} (Figure S8, SI), the ε-MnO_2 cathode delivers a capacity of 220−230 mAh g^{-1} for 50 cycles with a Coulombic efficiency around 95%, demonstrating that the transformed ε-MnO_2 is considerably stable. To evaluate the long-term cycling stability, the Zn/ε-MnO_2 cell is galvanostatically charged and discharged at the high rate of 500 mA g^{-1}. The cathode exhibits a discharge capacity of 132 mAh g^{-1} and sustains 92% of the initial discharge capacity over 500 cycles with a Coulombic efficiency approaching 99%. The electrochemical performance of our Zn/ε-MnO_2 cell is further compared to other aqueous Zn ion batteries, both energy density and cycling performance are remarkable among these aqueous Zn ion batteries reported before (Table S1, SI). In addition, as presented in Figure S9 (SI), the morphology of the cathode after 500 cycles remains porous nanosheets, demonstrating the excellent stability of the ε-MnO_2 cathode.

Electrode Reaction Mechanism. SEM, TEM, XRD, and XPS were applied to explore the morphological and structural evolution of the MnO_2 cathode during the charge and discharge processes of Zn/ε-MnO_2 aqueous batteries. The SEM image in Figure 6a shows that most of the cathode surface is covered by flakes with a dimension around several micrometers. The XRD peaks of the discharged product (Figure 6b) attributed to MnOOH (JCPDS 74-1049) are almost overwhelmed by the intense peaks from conductive graphite and consequent discharged products. The neighboring interlayer distances of 0.34 and 0.26 nm in the HREM image (Figure 6c) are well-assigned to the (210) and (020) planes of

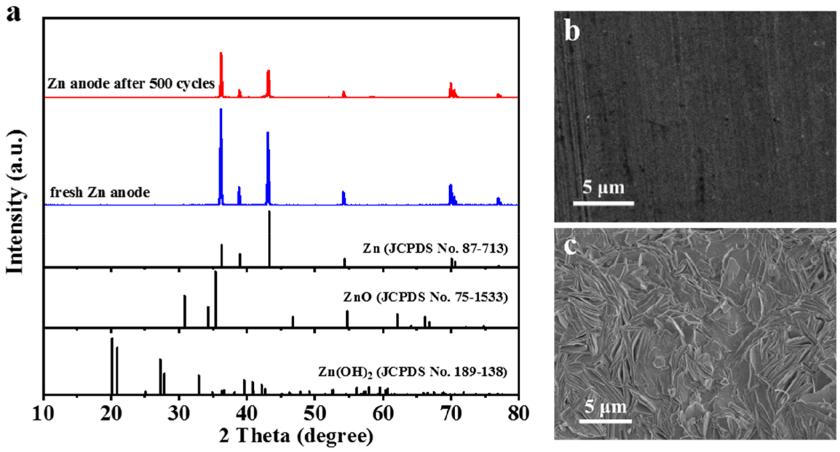

Figure 7. Characterization of Zn anode. (a) XRD patterns of pristine and cycled Zn anodes in 1 M $ZnSO_4$ + 1 M $MnSO_4$ electrolyte at 500 mA g^{-1}. SEM images of (b) pristine Zn anode and (c) Zn anode after 500 cycles at 500 mA g^{-1}.

monoclinic MnOOH, validating the formation of MnOOH during discharge. Meanwhile, STEM-EDS mappings (Figure 6d) of the discharged product display a uniform distribution of O and Mn without detection of Zn. Furthermore, the formation of MnOOH is also supported by the XPS result (Figure 6e). The two obvious peaks located at 641.9 eV for Mn $2p_{3/2}$ and 653.4 eV for Mn $2p_{1/2}$ are indicative of manganese atoms in the 3+ oxidation state.[46,47] The results manifest that ε-MnO_2 reacts with H^+ and converts to MnOOH during discharge. Nevertheless, the predominant XRD peaks of the discharged product correspond to $ZnSO_4[Zn(OH)_2]_3{\cdot}3H_2O$ (JCPDS 39-0689), combined with the SEM image, confirming that $ZnSO_4[Zn(OH)_2]_3{\cdot}3H_2O$ flakes are formed during the discharge process. Thus, it is speculated that the remaining OH^- react with $ZnSO_4$ and H_2O to keep electrolyte neutral upon H^+ intercalating into MnO_2 during discharge.

The Zn anode was also investigated to understand the excellent reversibility of the Zn/MnO_2 cell chemistry. Figure 7 presents XRD patterns and SEM images of virginal Zn sheet and cycled Zn anodes. All the XRD peaks of the virginal zinc plate as the anode before cycling (Figure 7a) are well-indexed to metal zinc. There are almost no obvious XRD signals of byproducts such as ZnO or $Zn(OH)_2$ in the XRD results of cycled Zn anodes, suggesting that redox of Zn/Zn^{2+} is the dominant reaction of the anode during cycling. Moreover, major peaks of Zn anode become weak after 500 cycles, consistent with the results in previous reports.[13,23] For comparison, Figure 7b,c illustrates the morphology of Zn anodes before and after cycling. It can be observed that the Zn anode still shows a dense, dendrite-free surface morphology after 500 cycles, indicating highly reversible plating/stripping of Zn metal, which is favorable for the long-term cycling stability of Zn/MnO_2 cells. In addition, neither dendritic morphology (Figure S10, SI) nor formation of byproducts such as ZnO or $Zn(OH)_2$ (Figure S11, SI) is observed after 50 cycles at a low current density of 100 mA g^{-1}.

■ CONCLUSION

In conclusion, we report Mn_3O_4 nanoparticles prepared via a low-cost, scalable, ball-milling method as cathode for aqueous ZIBs. The transformed akhtenskite MnO_2 from Mn_3O_4 achieves a high reversible capacity of 221 mAh g^{-1} at a current density of 100 mA g^{-1} and delivers a superior capacity retention of more than 92% after 500 cycles at a high rate of 500 mA g^{-1}. Meanwhile, the cell shows a specific energy of ∼288 Wh kg^{-1} (cathode only), which is much higher than that of commercial lead−acid batteries. The structural and morphological evolution of cathodes has been elucidated in detail. The mechanism involves two processes: the phase transition from Mn_3O_4 to ε-MnO_2 in the first 10 cycles at a low current density in 1 M $MnSO_4$ + 1 M $ZnSO_4$ aqueous electrolyte and the reversible conversion reaction between MnO_2 and MnOOH in the subsequent cycles. The combination of a low cost, scalable preparation and superior performance of the cathode material makes this approach a very promising candidate for the practical use of Zn/MnO_2 batteries. We also find a small drawback of the battery. It can self-discharge. At this stage, the exact reason leading to this issue is not clear. However, even with the self-discharging problem, the battery can still be applied to many situations where the long-time electricity storage is not a concern, e.g., electric buses, owing to its excellent electrochemical properties and safety features.

■ ASSOCIATED CONTENT

Ⓢ Supporting Information

The Supporting Information is available free of charge on the ACS Publications website at DOI: 10.1021/acssuschemeng.8b02502.

Digital photograph, SEM images, XRD patterns, and comparisons of electrochemical performances (PDF)

■ AUTHOR INFORMATION

Corresponding Authors

*J.C. e-mail: chenjitao@pku.edu.cn.
*J.Z. e-mail: junrong@pku.edu.cn.

ORCID

Jitao Chen: 0000-0002-2620-5587
Junrong Zheng: 0000-0002-4472-8576

Author Contributions

L.W. and J.Z. designed experiments. J.Z. supervised the project. L.W. L.X., and X.C. performed experiments. X.C., J.Z., J.C., and L.W. discussed experiments and results. L.W., J.C., and J.Z. prepared and revised the manuscript.

Notes

The authors declare no competing financial interest.

■ ACKNOWLEDGMENTS

This work was supported by the National Natural Science Foundation of China NSFC (NSFC-21673004, 21627805, 21821004, and 21673008) and MOST (2017YFA0204702) China and China Postdoctoral Science Foundation (grant 2017M610017).

■ REFERENCES

(1) Larcher, D.; Tarascon, J. M. Towards Greener and More Sustainable Batteries for Electrical Energy Storage. *Nat. Chem.* **2015**, *7*, 19−29.

(2) Armand, M.; Tarascon, J. M. Building Better Batteries. *Nature* **2008**, *451*, 652−657.

(3) Lu, Y.; Goodenough, J. B.; Kim, Y. Aqueous Cathode for Next-generation Alkali-ion Batteries. *J. Am. Chem. Soc.* **2011**, *133*, 5756−5759.

(4) Goodenough, J. B.; Kim, Y. Challenges for Rechargeable Li Batteries. *Chem. Mater.* **2010**, *22*, 587−603.

(5) Goodenough, J. B.; Park, K. S. The Li-ion Rechargeable Battery: A Perspective. *J. Am. Chem. Soc.* **2013**, *135*, 1167−1176.

(6) Dunn, B.; Kamath, H.; Tarascon, J. M. Electrical Energy Storage for the Grid: A Battery of Choices. *Science* **2011**, *334*, 928−934.

(7) Luo, J. Y.; Xia, Y. Y. Aqueous Lithium-ion Battery $LiTi_2(PO_4)_3$/$LiMn_2O_4$ with High Power and Energy Densities as well as Superior Cycling Stability. *Adv. Funct. Mater.* **2007**, *17*, 3877−3884.

(8) Tarascon, J. M.; Armand, M. Issues and Challenges Facing Rechargeable Lithium Batteries. *Nature* **2001**, *414*, 359−367.

(9) Cheng, F. Y.; Chen, J.; Gou, X. L.; Shen, P. W. High-Power Alkaline Zn-MnO_2 Batteries Using γ-MnO_2 Nanowires/Nanotubes and Electrolytic Zinc Powder. *Adv. Mater.* **2005**, *17*, 2753−2756.

(10) Li, G.; Yang, Z.; Jiang, Y.; Jin, C.; Huang, W.; Ding, X.; Huang, Y. Towards Polyvalent Ion Batteries: A Zinc-ion Battery Based on NASICON Structured $Na_3V_2(PO_4)_3$. *Nano Energy* **2016**, *25*, 211−217.

(11) Kundu, D.; Adams, B. D.; Duffort, V.; Vajargah, S. H.; Nazar, L. F. A High-capacity and Long-life Aqueous Rechargeable Zinc Battery Using A Metal Oxide Intercalation Cathode. *Nat. Energy* **2016**, *1*, 16119.

(12) Parker, J. F.; Chervin, C. N.; Pala, I. R.; Machler, M.; Burz, M. F.; Long, J. W.; Rolison, D. R. Rechargeable Nickel−3D Zinc Batteries: An Energy-dense, Safer Alternative to Lithium-ion. *Science* **2017**, *356*, 415−418.

(13) Zhang, N.; Cheng, F.; Liu, Y.; Zhao, Q.; Lei, K.; Chen, C.; Liu, X.; Chen, J. Cation-Deficient Spinel $ZnMn_2O_4$ Cathode in Zn-$(CF_3SO_3)_2$ Electrolyte for Rechargeable Aqueous Zn-Ion Battery. *J. Am. Chem. Soc.* **2016**, *138*, 12894−12901.

(14) Alfaruqi, M. H.; Mathew, V.; Song, J.; Kim, S.; Islam, S.; Pham, D. T.; Jo, J.; Kim, S.; Baboo, J. P.; Xiu, Z.; Lee, K.-S.; Sun, Y.-K.; Kim, J. Electrochemical Zinc Intercalation in Lithium Vanadium Oxide: A High-Capacity Zinc-Ion Battery Cathode. *Chem. Mater.* **2017**, *29*, 1684−1694.

(15) Kim, H.; Jeong, G.; Kim, Y. U.; Kim, J. H.; Park, C. M.; Sohn, H. J. Metallic Anodes for Next Generation Secondary Batteries. *Chem. Soc. Rev.* **2013**, *42*, 9011−9034.

(16) Zhang, L.; Chen, L.; Zhou, X.; Liu, Z. Morphology-Dependent Electrochemical Performance of Zinc Hexacyanoferrate Cathode for Zinc-Ion Battery. *Sci. Rep.* **2015**, *5*, 18263.

(17) Zhang, L.; Chen, L.; Zhou, X.; Liu, Z. Towards High-Voltage Aqueous Metal-Ion Batteries Beyond 1.5 V: The Zinc/Zinc Hexacyanoferrate System. *Adv. Energy Mater.* **2015**, *5*, 1400930.

(18) Liu, Z.; Pulletikurthi, G.; Endres, F. A Prussian Blue/Zinc Secondary Battery with a Bio-Ionic Liquid-Water Mixture as Electrolyte. *ACS Appl. Mater. Interfaces* **2016**, *8*, 12158−12164.

(19) Trocoli, R.; La Mantia, F. An Aqueous Zinc-ion Battery Based on Copper Hexacyanoferrate. *ChemSusChem* **2015**, *8*, 481−485.

(20) Jia, Z.; Wang, B.; Wang, Y. Copper Hexacyanoferrate with a Well-defined Open Framework as a Positive Electrode for Aqueous Zinc Ion Batteries. *Mater. Chem. Phys.* **2015**, *149−150*, 601−606.

(21) Gupta, T.; Kim, A.; Phadke, S.; Biswas, S.; Luong, T.; Hertzberg, B. J.; Chamoun, M.; Evans-Lutterodt, K.; Steingart, D. A. Improving the Cycle Life of a High-rate, High-potential Aqueous Dual-ion Battery Using Hyper-dendritic Zinc and Copper Hexacyanoferrate. *J. Power Sources* **2016**, *305*, 22−29.

(22) Kasiri, G.; Trócoli, R.; Bani Hashemi, A.; La Mantia, F. An Electrochemical Investigation of the Aging of Copper Hexacyanoferrate during the Operation in Zinc-ion Batteries. *Electrochim. Acta* **2016**, *222*, 74−83.

(23) Xu, C.; Li, B.; Du, H.; Kang, F. Energetic Zinc Ion Chemistry: the Rechargeable Zinc Ion Battery. *Angew. Chem., Int. Ed.* **2012**, *51*, 933−935.

(24) Lee, B.; Lee, H. R.; Kim, H.; Chung, K. Y.; Cho, B. W.; Oh, S. H. Elucidating the Intercalation Mechanism of Zinc Ions into Alpha-MnO_2 for Rechargeable Zinc Batteries. *Chem. Commun.* **2015**, *51*, 9265−9268.

(25) Lee, B.; Yoon, C. S.; Lee, H. R.; Chung, K. Y.; Cho, B. W.; Oh, S. H. Electrochemically-induced Reversible Transition from the Tunneled to Layered Polymorphs of Manganese Dioxide. *Sci. Rep.* **2014**, *4*, 6066.

(26) Alfaruqi, M. H.; Gim, J.; Kim, S.; Song, J.; Pham, D. T.; Jo, J.; Xiu, Z.; Mathew, V.; Kim, J. A Layered δ-MnO_2 Nanoflake Cathode with High Zinc-storage Capacities for Eco-friendly Battery Applications. *Electrochem. Commun.* **2015**, *60*, 121−125.

(27) Yuan, C.; Zhang, Y.; Pan, Y.; Liu, X.; Wang, G.; Cao, D. Investigation of the Intercalation of Polyvalent Cations (Mg^{2+}, Zn^{2+}) Into λ-MnO_2 for Rechargeable Aqueous Battery. *Electrochim. Acta* **2014**, *116*, 404−412.

(28) Alfaruqi, M. H.; Mathew, V.; Gim, J.; Kim, S.; Song, J.; Baboo, J. P.; Choi, S. H.; Kim, J. Electrochemically Induced Structural Transformation in a γ-MnO_2 Cathode of a High Capacity Zinc-Ion Battery System. *Chem. Mater.* **2015**, *27*, 3609−3620.

(29) Wei, C.; Xu, C.; Li, B.; Du, H.; Kang, F. Preparation and Characterization of Manganese Dioxides with Nano-sized Tunnel Structures for Zinc Ion Storage. *J. Phys. Chem. Solids* **2012**, *73*, 1487−1491.

(30) Jiang, B.; Xu, C.; Wu, C.; Dong, L.; Li, J.; Kang, F. Manganese Sesquioxide as Cathode Material for Multivalent Zinc Ion Battery with High Capacity and Long Cycle Life. *Electrochim. Acta* **2017**, *229*, 422−428.

(31) Pan, H.; Shao, Y.; Yan, P.; Cheng, Y.; Han, K. S.; Nie, Z.; Wang, C.; Yang, J.; Li, X.; Bhattacharya, P.; Mueller, K. T.; Liu, J. Reversible Aqueous Zinc/manganese Oxide Energy Storage from Conversion Reactions. *Nat. Energy* **2016**, *1*, 16039.

(32) Zhang, N.; Cheng, F.; Liu, J.; Wang, L.; Long, X.; Liu, X.; Li, F.; Chen, J. Rechargeable Aqueous Zinc-manganese Dioxide Batteries with High Energy and Power Densities. *Nat. Commun.* **2017**, *8*, 405.

(33) Liu, S.; Zhu, Y.; Xie, J.; Huo, Y.; Yang, H. Y.; Zhu, T.; Cao, G.; Zhao, X.; Zhang, S. Direct Growth of Flower-Like δ-MnO_2 on Three-Dimensional Graphene for High-Performance Rechargeable Li-O_2 Batteries. *Adv. Energy Mater.* **2014**, *4*, 1301960.

(34) Yan, J.; Fan, Z.; Wei, T.; Qian, W.; Zhang, M.; Wei, F. Fast and Reversible Surface Redox Reaction of Graphene−MnO_2 Composites as Supercapacitor Electrodes. *Carbon* **2010**, *48*, 3825−3833.

(35) Zhu, S.; Zhang, H.; Chen, P.; Nie, L.-H.; Li, C.-H.; Li, S.-K. Self-assembled Three-dimensional Hierarchical Graphene Hybrid Hydrogels with Ultrathin β-MnO_2 Nanobelts for High Performance Supercapacitors. *J. Mater. Chem. A* **2015**, 3, 1540−1548.

(36) Pendashteh, A.; Senokos, E.; Palma, J.; Anderson, M.; Vilatela, J. J.; Marcilla, R. Manganese Dioxide Decoration of Macroscopic Carbon Nanotube Fibers: From High-performance Liquid-based to All-solid-state Supercapacitors. *J. Power Sources* **2017**, *372*, 64−73.

(37) Dai, Y.; Wang, K.; Xie, J. From Spinel Mn_3O_4 to Layered Nanoarchitectures Using Electrochemical Cycling and the Distinctive Pseudocapacitive Behavior. *Appl. Phys. Lett.* **2007**, *90*, 104102.

(38) Komaba, S.; Tsuchikawa, T.; Ogata, A.; Yabuuchi, N.; Nakagawa, D.; Tomita, M. Nano-structured Birnessite Prepared by Electrochemical Activation of Manganese(III)-based Oxides for Aqueous Supercapacitors. *Electrochim. Acta* **2012**, *59*, 455−463.

(39) Nam, K. W.; Kim, S.; Lee, S.; Salama, M.; Shterenberg, I.; Gofer, Y.; Kim, J. S.; Yang, E.; Park, C. S.; Kim, J. S.; Lee, S. S.; Chang, W. S.; Doo, S. G.; Jo, Y. N.; Jung, Y.; Aurbach, D.; Choi, J. W. The High Performance of Crystal Water Containing Manganese Birnessite Cathodes for Magnesium Batteries. *Nano Lett.* **2015**, *15*, 4071−4079.

(40) Kim, S.; Nam, K. W.; Lee, S.; Cho, W.; Kim, J. S.; Kim, B. G.; Oshima, Y.; Kim, J. S.; Doo, S. G.; Chang, H.; Aurbach, D.; Choi, J. W. Direct Observation of an Anomalous Spinel-to-Layered Phase Transition Mediated by Crystal Water Intercalation. *Angew. Chem., Int. Ed.* **2015**, *54*, 15094−15099.

(41) Kim, S.; Lee, S.; Nam, K. W.; Shin, J.; Lim, S. Y.; Cho, W.; Suzuki, K.; Oshima, Y.; Hirayama, M.; Kanno, R.; Choi, J. W. On the Mechanism of Crystal Water Insertion during Anomalous Spinel-to-Birnessite Phase Transition. *Chem. Mater.* **2016**, *28*, 5488−5494.

(42) Nightingale, E. R., Jr. Phenomenological Theory of Ion Solvation - Effective Radii of Hydrated Ions. *J. Phys. Chem.* **1959**, *63*, 1381−1387.

(43) Tansel, B.; Sager, J.; Rector, T.; Garland, J.; Strayer, R. F.; Levine, L.; Roberts, M.; Hummerick, M.; Bauer, J. Significance of Hydrated Radius and Hydration Shells on Ionic Permeability during Nanofiltration in Dead End and Cross Flow Modes. *Sep. Purif. Technol.* **2006**, *51*, 40−47.

(44) Delmer, O.; Balaya, P.; Kienle, L.; Maier, J. Enhanced Potential of Amorphous Electrode Materials: Case Study of RuO_2. *Adv. Mater.* **2008**, *20*, 501−505.

(45) Zhong, K.; Zhang, B.; Luo, S.; Wen, W.; Li, H.; Huang, X.; Chen, L. Investigation on Porous MnO Microsphere Anode for Lithium Ion Batteries. *J. Power Sources* **2011**, *196*, 6802−6808.

(46) Shao, L.; Zhao, Q.; Chen, J. MnOOH Nanorods as High-performance Anodes for Sodium Ion Batteries. *Chem. Commun.* **2017**, *53*, 2435−2438.

(47) Biesinger, M. C.; Payne, B. P.; Grosvenor, A. P.; Lau, L. W. M.; Gerson, A. R.; Smart, R. S. C. Resolving Surface Chemical States in XPS Analysis of First Row Transition Metals, Oxides and Hydroxides: Cr, Mn, Fe, Co and Ni. *Appl. Surf. Sci.* **2011**, *257*, 2717−2730.